

# Pulse compression in adiabatically tapered silicon photonic wires

Spyros Lavdas,<sup>1</sup> Jeffrey B. Driscoll,<sup>2</sup> Richard R. Grote,<sup>2</sup>  
Richard M. Osgood, Jr.,<sup>2</sup> and Nicolae C. Panoiu<sup>1,\*</sup>

<sup>1</sup>*Department of Electronic and Electrical Engineering, University College London, Torrington Place, London WC1E 7JE, UK*

<sup>2</sup>*Microelectronics Sciences Laboratories, Columbia University, New York, NY 10027, USA*

[\\*n.panoiu@ucl.ac.uk](mailto:n.panoiu@ucl.ac.uk)

**Abstract:** We present a comprehensive analysis of pulse compression in adiabatically tapered silicon photonic wire waveguides (Si-PhWWGs), both at telecom ( $\lambda \sim 1.55 \mu\text{m}$ ) and mid-IR ( $\lambda \gtrsim 2.1 \mu\text{m}$ ) wavelengths. Our theoretical and computational study is based on a rigorous model that describes the coupled dynamics of the optical field and photogenerated free carriers, as well as the influence of the physical and geometrical parameters of the Si-PhWWGs on these dynamics. We consider both the soliton and non-soliton pulse propagation regimes, rendering the conclusions of this study relevant to a broad range of experimental settings and practical applications. In particular, we show that by engineering the linear and nonlinear optical properties of Si-PhWWGs through adiabatically varying their width, one can achieve more than  $10\times$  pulse compression in millimeter-long waveguides. The inter-dependence between the pulse characteristics and compression efficiency is also discussed.

© 2014 Optical Society of America

**OCIS codes:** (130.4310) Nonlinear integrated optics; (230.4320) Nonlinear optical devices; (230.7380) Waveguides, channeled; (320.5520) Pulse compression; (320.5540) Pulse shaping.

---

## References and links

1. E. B. Treacy, "Optical pulse compression with diffraction gratings," *IEEE J. Quantum Electron.* **QE 5**, 454–458 (1969).
2. O. E. Martinez, J. P. Gordon, and R. L. Fork, "Negative group-velocity dispersion using refraction," *J. Opt. Soc. Am. A* **1**, 1003–1006 (1984).
3. A. M. Weiner, "Femtosecond pulse shaping using spatial light modulators," *Rev. Sci. Instrum.* **71**, 1929–1960 (2000).
4. G. Imeshev, A. Galvanauskas, D. Harter, M. A. Arbore, M. Proctor, and M. M. Fejer, "Engineerable femtosecond pulse shaping by second-harmonic generation with Fourier synthetic quasi-phase-matching gratings," *Opt. Lett.* **23**, 864–866 (1998).
5. N. J. Doran and D. Wood, "Nonlinear-optical loop mirror," *Opt. Lett.* **13**, 56–58 (1988).
6. K. Smith, N. J. Doran, and P. G. J. Wigley, "Pulse shaping, compression, and pedestal suppression employing a nonlinear-optical loop mirror," *Opt. Lett.* **15**, 1294–1296 (1990).
7. M. D. Pelusi, Y. Matsui, and A. Suzuki, "Pedestal suppression from compressed femtosecond pulses using a nonlinear fiber loop mirror," *IEEE J. Quantum Electron.* **35**, 867–874 (1999).
8. W. J. Tomlinson, R. H. Stolen, and C. V. Shank, "Compression of optical pulses chirped by self-phase modulation in fibers," *J. Opt. Soc. Am. B* **1**, 139–149 (1984).
9. M. Nisoli, S. De Silvestri, O. Svelto, R. Szipocs, K. Ferencz, C. Spielmann, S. Sartania, and F. Krausz, "Compression of high-energy laser pulses below 5 fs," *Opt. Lett.* **22**, 522–524 (1997).
10. J. T. Manassah, "Pulse compression of an induced-phase-modulated weak signal," *Opt. Lett.* **13**, 755–757 (1988).
11. G. P. Agrawal, P. L. Baldeck, and R. R. Alfano, "Optical wave breaking and pulse compression due to cross-phase modulation in optical fibers," *Opt. Lett.* **14**, 137–139 (1989).

12. L. F. Mollenauer, R. H. Stolen, J. P. Gordon, and W. J. Tomlinson, "Extreme picosecond pulse narrowing by means of soliton effect in single-mode optical fibers," *Opt. Lett.* **8**, 289–291 (1983).
13. K. A. Ahmed, K. C. Chan, and H. F. Liu, "Femtosecond pulse generation from semiconductor laser using the soliton effect compression technique," *IEEE J. Sel. Top. Quantum Electron.* **1**, 592–600 (1995).
14. M. D. Pelusi and H. F. Liu, "Higher order soliton pulse compression in dispersion-decreasing optical fibers," *IEEE J. Quantum Electron.* **33**, 1430–1439 (1997).
15. A. A. Amorim, M. V. Tognetti, P. Oliveira, J. L. Silva, L. M. Bernardo, F. X. Kartner, and H. M. Crespo, "Sub-two-cycle pulses by soliton self-compression in highly nonlinear photonic crystal fibers," *Opt. Lett.* **34**, 3851–3853 (2009).
16. A. C. Peacock, "Mid-IR soliton compression in silicon optical fibers and fiber tapers," *Opt. Lett.* **37**, 818–820 (2012).
17. S. V. Chernikov, E. M. Dianov, D. J. Richardson, and D. N. Payne, "Soliton pulse compression in dispersion-decreasing fiber," *Opt. Lett.* **18**, 476–478 (1993).
18. M. Nakazawa, E. Yoshida, H. Kubota, and Y. Kimura, "Generation of a 170 fs, 10 GHz transform-limited pulse train at 1.55  $\mu\text{m}$  using a dispersion decreasing, erbium-doped active soliton compressor," *Electron. Lett.* **30**, 2038–2040 (1994).
19. J. Hu, B. S. Marks, C. R. Menyuk, J. Kim, T. F. Carruthers, B. M. Wright, T. F. Taunay, and E. J. Friebele, "Pulse compression using a tapered microstructure optical fiber," *Opt. Express* **14**, 4026–4036 (2006).
20. M. L. V. Tse, P. Horak, J. H. V. Price, F. Poletti, F. He, and D. J. Richardson, "Pulse compression at 1.06  $\mu\text{m}$  in dispersion-decreasing holey fibers," *Opt. Lett.* **31**, 3504–3506 (2006).
21. A. C. Peacock, "Soliton propagation in tapered silicon core fibers," *Opt. Lett.* **35**, 3697–3699 (2010).
22. L. Tong, R. Gattass, J. Ashcom, S. He, J. Lou, M. Shen, I. Maxwell, and E. Mazur, "Subwavelength-diameter silica wires for low-loss optical wave guiding," *Nature* **426**, 816–819 (2003).
23. M. Foster, A. Gaeta, Q. Cao, and R. Trebino, "Soliton-effect compression of supercontinuum to few-cycle durations in photonic nanowires," *Opt. Express* **13**, 6848–6855 (2005).
24. A. Blanco-Redondo, C. Husko, D. Eades, Y. Zhang, J. Li, T. F. Krauss, and B. J. Eggleton, "Observation of soliton compression in silicon photonic crystals," *Nat. Commun.* **5**, 3160 (2014).
25. K. K. Lee, D. R. Lim, H. C. Luan, A. Agarwal, J. Foresi, and L. C. Kimerling, "Effect of size and roughness on light transmission in a Si/SiO<sub>2</sub> waveguide: Experiments and model," *Appl. Phys. Lett.* **77**, 1617–1619 (2000).
26. R. U. Ahmad, F. Pizzuto, G. S. Camarda, R. L. Espinola, H. Rao, and R. M. Osgood, "Ultra-compact corner-mirrors and T-branches in silicon-on-insulator," *IEEE Photon. Technol. Lett.* **14**, 65–67 (2002).
27. Q. Lin, O. J. Painter, and G. Agrawal, "Nonlinear optical phenomena in silicon waveguides: modelling and applications," *Opt. Express* **15**, 16604–16644 (2007).
28. J. I. Dadap, N. C. Panoiu, X. G. Chen, I. W. Hsieh, X. P. Liu, C. Y. Chou, E. Dulkeith, S. J. McNab, F. N. Xia, W. M. J. Green, L. Sekaric, Y. A. Vlasov, and R. M. Osgood, "Nonlinear-optical phase modification in dispersion-engineered Si photonic wires," *Opt. Express* **16**, 1280–1299 (2008).
29. R. M. Osgood, N. C. Panoiu, J. I. Dadap, X. Liu, X. Chen, I-W. Hsieh, E. Dulkeith, W. M. J. Green, and Y. A. Vlasov, "Engineering nonlinearities in nanoscale optical systems: physics and applications in dispersion-engineered silicon nanophotonic wires," *Adv. Opt. Photon.* **1**, 162–235 (2009).
30. X. Chen, N. C. Panoiu, I. W. Hsieh, J. I. Dadap, and R. M. Osgood, "Third-order dispersion and ultrafast-pulse propagation in silicon wire waveguides," *IEEE Photon. Technol. Lett.* **18**, 2617–2619 (2006).
31. M. Mohebbi, "Silicon photonic nanowire soliton-effect compressor at 1.5  $\mu\text{m}$ ," *IEEE Photon. Technol. Lett.* **20**, 921–923 (2008).
32. N. C. Panoiu, X. Chen, and R. M. Osgood, "Modulation instability in silicon photonic nanowires," *Opt. Lett.* **31**, 3609–3611 (2006).
33. M. A. Foster, A. C. Turner, J. E. Sharping, B. S. Schmidt, M. Lipson, and A. L. Gaeta, "Broad-band optical parametric gain on a silicon photonic chip," *Nature* **441**, 960–963 (2006).
34. X. Liu, R. M. Osgood, Y. A. Vlasov, and W. M. J. Green, "Mid-infrared optical parametric amplifier using silicon nanophotonic waveguides," *Nat. Photonics* **4**, 557–560 (2010).
35. O. Boyraz, P. Koonath, V. Raghunathan, and B. Jalali, "All optical switching and continuum generation in silicon waveguides," *Opt. Express* **12**, 4094–4102 (2004).
36. I. W. Hsieh, X. Chen, X. P. Liu, J. I. Dadap, N. C. Panoiu, C. Y. Chou, F. Xia, W. M. Green, Y. A. Vlasov, and R. M. Osgood, "Supercontinuum generation in silicon photonic wires," *Opt. Express* **15**, 15242–15249 (2007).
37. L. Yin, Q. Lin, and G. P. Agrawal, "Soliton fission and supercontinuum generation in silicon waveguides," *Opt. Lett.* **32**, 391–393 (2007).
38. N. C. Panoiu, X. Liu, and R. M. Osgood, "Self-steepening of ultrashort pulses in silicon photonic nanowires," *Opt. Lett.* **34**, 947–949 (2009).
39. H. Fukuda, K. Yamada, T. Shoji, M. Takahashi, T. Tsuchizawa, T. Watanabe, J. Takahashi, and S. Itabashi, "Four-wave mixing in silicon wire waveguides," *Opt. Express* **13**, 4629–4637 (2005).
40. R. Espinola, J. Dadap, R. M. Osgood, Jr., S. McNab, and Y. Vlasov, "C-band wavelength conversion in silicon photonic wire waveguides," *Opt. Express* **13**, 4341–4349 (2005).
41. M. A. Foster, A. C. Turner, R. Salem, M. Lipson, and A. L. Gaeta, "Broad-band continuous-wave parametric

- wavelength conversion in silicon nanowaveguides,” *Opt. Express* **15**, 12949–12958 (2007).
42. S. Zlatanovic, J. S. Park, S. Moro, J. M. C. Boggio, I. B. Divliansky, N. Alic, S. Mookherjea, and S. Radic, “Mid-infrared wavelength conversion in silicon waveguides using ultracompact telecom-band-derived pump source,” *Nat. Photonics* **4**, 561–564 (2010).
  43. J. B. Driscoll, N. Ophir, R. R. Grote, J. I. Dadap, N. C. Panoiu, K. Bergman, and R. M. Osgood, “Width-modulation of Si photonic wires for quasi-phase-matching of four-wave-mixing: experimental and theoretical demonstration,” *Opt. Express* **20**, 9227–9242 (2012).
  44. S. Lavdas, J. B. Driscoll, H. Jiang, R. R. Grote, R. M. Osgood, and N. C. Panoiu, “Generation of parabolic similaritons in tapered silicon photonic wires: comparison of pulse dynamics at telecom and mid-infrared wavelengths,” *Opt. Lett.* **38**, 3953–3956 (2013).
  45. X. Chen, N. C. Panoiu, and R. M. Osgood, “Theory of Raman-mediated pulsed amplification in silicon-wire waveguides,” *IEEE J. Quantum Electron.* **42**, 160–170 (2006).
  46. N. C. Panoiu, J. F. McMillan, and C. W. Wong, “Theoretical analysis of pulse dynamics in silicon photonic crystal wire waveguides,” *IEEE J. Sel. Top. Quantum Electron.* **16**, 257–266 (2010).
  47. M. P. Nezhad, O. Bondarenko, M. Khajavikhan, A. Simic, and Y. Fainman, “Etch-free low loss silicon waveguides using hydrogen silsesquioxane oxidation masks,” *Opt. Express* **19**, 18827–18832 (2011).
  48. G. Li, J. Yao, Y. Luo, H. Thacker, A. Mekis, X. Zheng, I. Shubin, J.-H. Lee, K. Raj, J. E. Cunningham, and A. V. Krishnamoorthy, “Ultralow-loss, high-density SOI optical waveguide routing for macrochip interconnects,” *Opt. Express* **20**, 12035–12039 (2012).
  49. G. P. Agrawal, *Nonlinear Fiber Optics* (Academic, 2007).
  50. J. Santhanam and G. P. Agrawal, “Raman-induced spectral shifts in optical fibers: general theory based on the moment method,” *Opt. Commun.* **222**, 413–420 (2003).

## 1. Introduction

Optical pulse compression techniques provide an essential functionality on which a broad array of optics and photonic applications rely, including broadband communication systems, nonlinear optics, optical coherence tomography for cross-sectional tissue imaging, materials processing, and nonlinear microscopy. Several schemes for optical pulse compression, based on linear and nonlinear optical techniques, have been proposed, among the most successful and widely adopted being pulse compressors employing diffraction grating pairs [1–3], synthetic quasi-phase-matching gratings [4], interferometric systems based on nonlinear optical loop mirrors [5–7], self-phase modulation (SPM) and cross-phase modulation induced pulse compression [8–11], higher-order soliton pulse compression [12–16], and adiabatic soliton compression [17, 18]. The efficiency of these techniques can significantly be improved by tailoring the linear and nonlinear physical properties of the optical medium in which the pulse propagates, so that pulses with predesigned temporal and spectral properties are generated. In particular, efficient pulse compression have been demonstrated in several types of dispersion-engineered optical waveguides, such as dispersion-decreasing fibers [14, 17, 18], tapered holey fibers [19, 20], sub-micron tapered fibers [16, 21–23], and photonic crystal waveguides [24]. Among all these alternative solutions, sub-wavelength silicon (Si) devices are at the center of intense current research efforts geared towards achieving pulse compression at optical chip-scale.

Tapered Si photonic wire waveguides (Si-PhWWGs) with subwavelength transverse size [25, 26] are photonic devices ideally suited for dispersion engineering. Thus, due to the combined effects of the large difference between the index of refraction of the Si core ( $n_{\text{Si}} \approx 3.4$ ) and that of the cladding (usually air,  $n_{\text{air}} = 1$ ) and the subwavelength nature of the cross-sectional area of the waveguide, variations in the transverse size of the waveguide as small as only a few percent of the operating wavelength can induce changes of the mode propagation constant,  $\beta$ , which are large enough to significantly affect the temporal and spectral properties of pulses that propagate in such photonic wires. In particular, by simply varying the waveguide width, one can readily design Si-PhWWGs whose frequency dispersion changes between normal dispersion, where the second-order dispersion coefficient,  $\beta_2(\omega) = \beta''(\omega) > 0$ , and anomalous dispersion ( $\beta_2 < 0$ ), or waveguides that possess multiple zero-dispersion points, defined by  $\beta_2(\omega) = 0$ . Equally important, the large intrinsic third-order nonlinearity of Si, in conjunction with the

strong field confinement achievable in high-index contrast waveguides, make it possible to attain strong nonlinear pulse reshaping at low optical power. More specifically, the dispersion length,  $L_D$ , and the nonlinear length,  $L_{nl}$ , of Si-PhWWGs can be more than four orders of magnitude smaller than in silica fibers [27–29]. As a result, linear and nonlinear optical effects that normally require kilometer-long optical fibers to be observed can be achieved in millimeter-long Si devices. Examples of such effects include soliton pulse compression [30, 31], modulational instability [32], parametric amplification [33, 34], supercontinuum generation [35–37], pulse self-steepening [38], four-wave mixing [39–43], and generation of parabolic similaritons [44].

In this work, we theoretically analyze the compression of optical pulses upon propagation in tapered Si-PhWWGs. We focus primarily on two compression methods: the soliton compression technique and pulse compression in Si-PhWWGs whose group-velocity dispersion (GVD) coefficient  $\beta_2$  changes sign during pulse propagation. While the first approach can be employed only at relatively large peak pulse power, namely in the soliton propagation regime, the latter one can be used to compress pulses whose power is below the soliton formation threshold as well. Our theoretical model rigorously describes the effects of the adiabatic variation of the cross-section of Si-PhWWGs on the pulse dynamics by fully accounting for the influence of this variation on the linear and nonlinear optical coefficients of the waveguide. For the sake of completeness, we consider the pulse dynamics at the optical communications wavelength,  $\lambda \sim 1.55 \mu\text{m}$ , and at mid-infrared wavelengths,  $\lambda \gtrsim 2.1 \mu\text{m}$ .

Our paper is organized as follows: in Section 2 we introduce the physical model we use to describe the coupled dynamics of the optical field and free carriers (FCs) upon pulse propagation in tapered Si-PhWWGs. In order to gain a deeper understanding of the main physics governing these dynamics we also introduce a simplified semi-analytical model based on the method of moments, namely a model that describes the pulse dynamics simply as the evolution with the propagation distance of a small set of physical parameters that define the pulse. Then, in Section 3, we present the optical properties of the tapered Si-PhWWGs considered in this work. In Section 4 and Section 5 we analyze the characteristics of optical pulse compression achieved via the soliton compression technique and by using waveguides with sign-changing dispersion, respectively, as well as a comparison between the pulse compression efficiency of these two methods. The main conclusions of this work are summarized in Section 6.

## 2. Theoretical models for pulse propagation in subwavelength tapered Si waveguides

In this section, we introduce a theoretical model that describes the propagation of ultrashort pulses in tapered Si-PhWWGs and a simplified semi-analytical mathematical model, based on the method of moments, which reduces the pulse evolution to a particle-like dynamics.

### 2.1. Theoretical model for propagation of ultrashort optical pulses

We describe the optical pulse dynamics by using a rigorous theoretical model based on the slowly-varying envelope approximation, which incorporates all relevant linear and nonlinear optical effects pertaining to the pulse propagation in tapered Si-PhWWGs, including linear losses, modal dispersive effects up to the third-order, FC frequency dispersion and FC absorption, SPM, two-photon absorption (TPA), and pulse self-steepening, as well as the associated FC dynamics [38, 43–46]. Mathematically, the dynamics of the optical field are described by the following partial differential equation:

$$i \frac{\partial u}{\partial z} + \sum_{n=1}^3 \frac{i^n \beta_n(z)}{n!} \frac{\partial^n u}{\partial t^n} = - \frac{ic\kappa(z)}{2nv_g(z)} \alpha(z)u - \frac{\omega\kappa(z)}{nv_g(z)} \delta n(z)u - \gamma(z) \left[ 1 + i\tau_s(z) \frac{\partial}{\partial t} \right] |u|^2 u, \quad (1)$$

where  $u(z, t)$  is the pulse envelope, measured in  $\sqrt{\text{W}}$ ,  $z$  and  $t$  are the distance along the Si-PhWWGs and time, respectively,  $\beta_n(z) = d^n \beta / d\omega^n$  is the  $n$ th order dispersion coefficient,

$\kappa(z)$  measures the overlap between the optical mode and the (Si) active area of the waveguide,  $v_g(z)$  is the group-velocity,  $\delta n(z)$  and  $\alpha(z)$  are the FC-induced refractive index change and losses, respectively, and are given by  $\delta n(z) = -(e^2/2\epsilon_0 n \omega^2) [N(z)/m_{ce}^* + N(z)^{0.8}/m_{ch}^*]$  and  $\alpha(z) = e^3 N(z) (1/\mu_e m_{ce}^{*2} + 1/\mu_h m_{ch}^{*2}) / \epsilon_0 c n \omega^2$ , where  $N$  is the FC density,  $m_{ce}^* = 0.26m_0$  ( $m_{ch}^* = 0.39m_0$ ) is the electrons (holes) effective mass, with  $m_0$  the electron mass, and  $\mu_e = 850 \text{ cm}^2/(\text{V s})$  [ $\mu_h = 210 \text{ cm}^2/(\text{V s})$ ] the electron (hole) mobility. The nonlinear properties of the waveguide are described by the nonlinear coefficient,  $\gamma(z) = 3\omega\Gamma(z)/4\epsilon_0 A(z)v_g^2(z)$ , and the shock time scale, *i.e.* the characteristic response time of the nonlinearity,  $\tau_s(z) = \partial \ln \gamma(z) / \partial \omega$ , where  $A(z)$  and  $\Gamma(z)$  are the cross-sectional area and the effective third-order susceptibility of the waveguide, respectively. Nonlinear optical effects higher than the third-order are not considered here; however, at high peak power they might become important. Note that in Eq. (1) linear losses are neglected because the loss length is significantly larger than the waveguide lengths considered in our study,  $L < 10 \text{ cm}$ . Specifically, the loss coefficient of Si waveguides is  $\alpha_i < 0.4 \text{ dB/cm}$  [47], waveguides with losses as small as  $0.026 \text{ dB/cm}$  being recently reported [48]. For comparison, the loss length corresponding to  $0.1 \text{ dB/cm}$  is  $43.4 \text{ cm}$ . The theoretical model is completed by a rate equation, which governs the dynamics of FCs:

$$\frac{\partial N(z,t)}{\partial t} = -\frac{N(z,t)}{t_c} + \frac{3\Gamma''(z)}{4\epsilon_0 \hbar A^2(z) v_g^2(z)} |u(z,t)|^4, \quad (2)$$

where  $\Gamma''$  ( $\Gamma'$ ) is the imaginary (real) part of  $\Gamma$  and  $t_c$  is the FC relaxation time. In our analysis we considered  $t_c = 1 \text{ ns}$  [29].

## 2.2. Semi-analytical model based on the method of moments

While Eqs. (1) and (2) provide detailed information about the pulse evolution, it is often more convenient to use a simplified approach based on a particle-like description of the pulse dynamics. In this approximation, also called the method of moments [49], the pulse is characterized by a relatively small number of parameters, which are assumed to change adiabatically during its propagation. The physical quantities used in our analysis are defined as follows:

$$E = \int_{-\infty}^{\infty} |u|^2 dt, \quad (3a)$$

$$\tau^2 = \frac{\delta}{E} \int_{-\infty}^{\infty} (t-T)^2 |u|^2 dt, \quad (3b)$$

$$C = \frac{i\delta}{2E} \int_{-\infty}^{\infty} (t-T) (u^* u_t - u u_t^*) dt, \quad (3c)$$

$$\Omega = \frac{i}{2E} \int_{-\infty}^{\infty} (u^* u_t - u u_t^*) dt, \quad (3d)$$

$$T = \frac{1}{E} \int_{-\infty}^{\infty} t |u|^2 dt, \quad (3e)$$

where  $E$ ,  $\tau$ ,  $C$ ,  $\Omega$ , and  $T$  are the pulse energy, pulse width, chirp coefficient, shift of the pulse carrier frequency, and temporal shift of the pulse, respectively. The parameter  $\delta$  depends on the specific shape of the pulse, being equal to  $12/\pi^2$  and  $2$  for secant-hyperbolic and Gaussian pulses, respectively. These pulses are defined as:

$$u_s(t, z=0) = \sqrt{\frac{E}{2\tau}} \operatorname{sech}\left(\frac{t-T}{\tau}\right) e^{-i\Omega(t-T) - iC\frac{(t-T)^2}{2\tau^2}}, \quad (4a)$$

$$u_G(t, z=0) = \sqrt{\frac{E}{\pi\tau}} e^{-i\Omega(t-T) - (1+iC)\frac{(t-T)^2}{2\tau^2}}. \quad (4b)$$

The pulse width and its full-width at half-maximum (FWHM),  $T_{\text{FWHM}}$ , are related by  $T_{\text{FWHM}} = 1.763\tau$  and  $T_{\text{FWHM}} = 1.665\tau$  for secant-hyperbolic and Gaussian pulses, respectively.

To determine the pulse dynamics one calculates the  $z$ -derivative of the quantities in Eqs. (3a)–(3e) and use Eq. (1) to eliminate from the integrands the partial derivatives wrt  $z$  of  $u(z, t)$ . This leads to the following nonlinear system of ordinary differential equations (see also [50]):

$$\frac{d\mathbf{F}(z)}{dz} = \mathbf{A}(E, \tau, C, \Omega, T), \quad (5)$$

where  $\mathbf{F}(z) = [E(z), \tau(z), C(z), \Omega(z), T(z)]^\top$  is a column vector containing the  $z$ -dependent parameters that characterize the pulse and  $\mathbf{A}$  is a column vector that depends on these parameters. The components of this vector depend on the specific shape of the pulse, their expressions for the two particular cases considered in this work being provided in the Appendix. Equation (5) is solved by using a standard Runge-Kutta method of 5th order. Note that in our derivation of Eq. (5) the influence of FCs on the pulse dynamics is accounted for only through the TPA and nonlinear frequency dispersion terms in Eq. (1), that is, we have neglected the FC absorption and FC dispersion effects. While this is a good approximation for femtosecond pulses, in which case the amount of generated FCs is small, the influence of these FC related effects on picosecond pulses should not be neglected [29]. This means that the conclusions derived by using this simplified model must be validated by a full numerical integration of the rigorous theoretical model defined by Eqs. (1) and (2).

### 3. Dispersion maps of linear and nonlinear parameters of tapered silicon waveguides

We assume that optical pulses propagate in a Si waveguide with rectangular core cross-section. The height of the waveguide is constant,  $h = 250$  nm, whereas its width,  $w$ , varies adiabatically along the waveguide. More exactly, this means that the condition  $\frac{\lambda}{w} \frac{dw}{dz} \ll n_{\text{eff}} - 1$  must be satisfied, where  $\lambda$  and  $n_{\text{eff}}$  are the wavelength and effective refractive index of the mode, respectively. The Si core is assumed to be buried in silica.

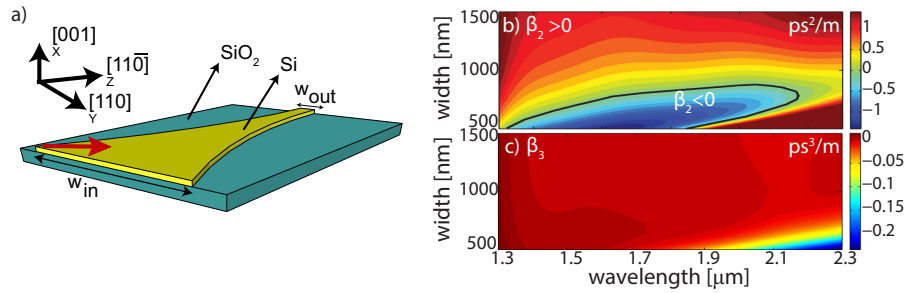


Fig. 1. a) Sketch of a Si-PhWWG oriented along the  $1\bar{1}0$  direction (red arrow). Dispersion maps of b) second-order,  $\beta_2$ , and c) third-order dispersion coefficient,  $\beta_3$ . The black contour corresponds to zero-GVD,  $\beta_2(\lambda, w) = 0$ .

In order to determine the wavelength and width dependence of the waveguide parameters we calculated the fundamental mode (TE-like) of the waveguide and its propagation constant for 51 widths, ranging from 500 nm to 1500 nm, with the wavelength spanning the spectral domain from 1.3  $\mu\text{m}$  to 2.3  $\mu\text{m}$ . Note that in this spectral domain the waveguide is single mode. The propagation constant was then fitted with a 12th degree polynomial, for each value of  $w$ , the higher-order dispersion coefficients,  $\beta_n$ , being determined by simply taking the corresponding derivatives wrt  $\lambda$ . A similar procedure was used to determine the frequency dispersion of the

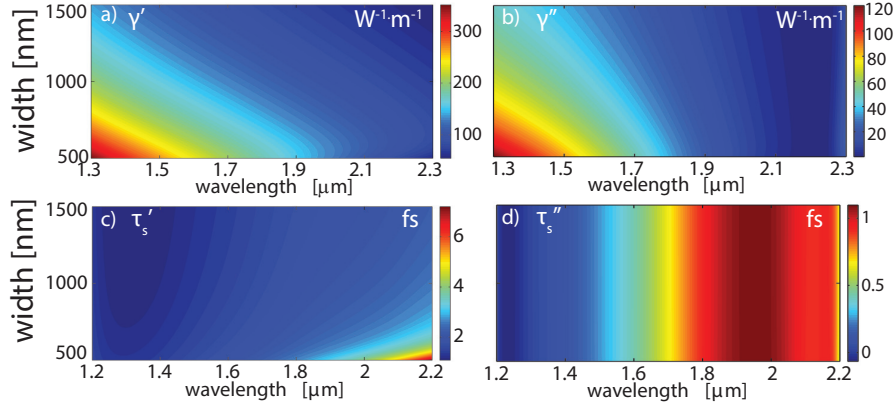


Fig. 2. Dispersion maps of a) real and b) imaginary part of the nonlinear coefficient,  $\gamma$ , and the dispersion maps of c) real and d) imaginary part of the shock-time coefficient,  $\tau_s$ .

other optical coefficients of the tapered Si-PhWWG, namely  $\gamma(\lambda)$ ,  $\kappa(\lambda)$ , and  $\tau_s(\lambda)$ . Polynomial interpolation was used to calculate the values of these coefficients when the waveguide width was different from our 51 chosen values (see also [44]).

The dispersion maps of the linear and nonlinear optical coefficients of the tapered Si-PhWWGs considered in this study are summarized in Figs. 1 and 2, respectively. These maps reveal an important property of these waveguides, namely in a broad range of frequencies the dispersion regime can be switched between normal and anomalous by simply varying the waveguide width. These two regimes are separated by a zero-dispersion curve defined by  $\beta_2(\lambda) = 0$ , depicted in Fig. 1(b) as a black contour. Note that in the soliton regime the waveguide nonlinearity is relatively large, as per Fig. 2(a), because this regime is achieved for small  $w$ , when the optical field is strongly confined in the Si core. This means that these Si photonic wires readily provide the main ingredients needed for soliton pulse compression in dispersion-varying optical guiding devices. Moreover, since we investigate the compression of pulses down to just a few hundreds of femtoseconds, the influence of third-order dispersion (TOD) and frequency dispersion of the nonlinearity must be accounted for. The dispersion map of the TOD coefficient,  $\beta_3(\lambda)$ , is shown in Fig. 1(c), whereas the dispersive properties of the nonlinearity dispersion are illustrated in Figs. 2(c) and 2(d).

#### 4. Soliton pulse compression in dispersion-varying tapered silicon waveguides

Generally, there are two main methods used to compress pulses that propagate in the soliton regime. The first is based on the particle-like propagation characteristics of solitons. Specifically, single solitons are propagated in an optical medium whose dispersion and nonlinearity change adiabatically, which leads to a slowly decrease of the soliton width. The drawback of this method is that optical losses can affect its efficiency, which in the context of Si-PhWWGs is an even more important aspect. The second method relies on the fact that higher-order solitons evolve periodically as they propagate, so that at certain distances their width is much smaller than that of the initial soliton. By properly choosing the waveguide length, large pulse compression is achieved. Because it is much more effective, we study here only this latter method.

To begin with, we launch a secant-hyperbolic pulse described by Eq. (4a) with  $\lambda = 1.55 \mu\text{m}$  in a tapered Si-PhWWG. The longitudinal  $z$ -variation of the width profile of the waveguide is assumed to be  $w(z) = w_{\text{in}} + (w_{\text{out}} - w_{\text{in}}) \tanh(az) / \tanh(aL)$ , where  $w_{\text{in}} = 700 \text{ nm}$  and  $w_{\text{out}} = 660 \text{ nm}$ , are the initial and final width of the waveguide, respectively,  $L = 9 \text{ cm}$  is the

waveguide length, and  $a = 80 \text{ m}^{-1}$ . This choice of the taper parameters ensures that the adiabaticity criterion,  $\lambda a \ll 1$ , is clearly satisfied and that the pulse propagates throughout into the soliton regime,  $\beta_2 < 0$ . The width of the input pulse is  $\tau = 180 \text{ fs}$  and the input peak power,  $P_0 = 1.4 \text{ W}$ , which means that the initial value of the soliton number,  $N_s$ , defined as  $N_s^2 = L_D/L_{\text{nl}} = \gamma P_0 \tau^2 / |\beta_2|$ , is  $N_s = 10$ .

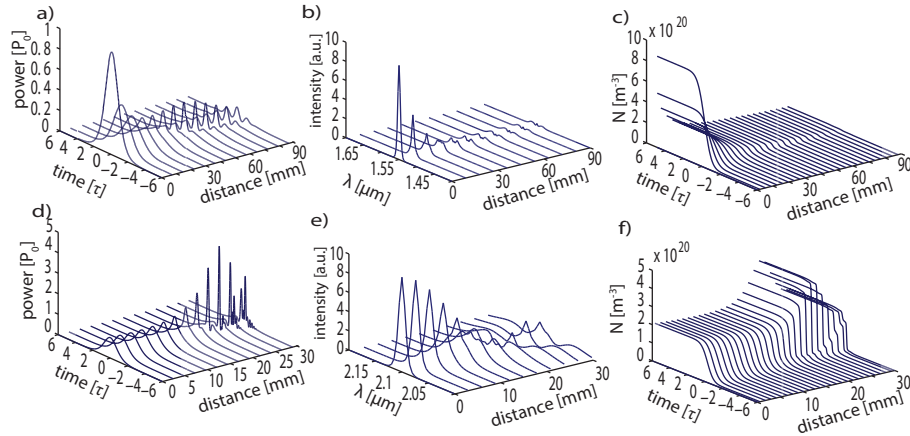


Fig. 3. Temporal [a) and d)] and spectral [b) and e)] pulse evolution in a tapered Si-PhWWG (see text for taper and pulse parameters) and the corresponding free-carriers dynamics [c) and f)]. Top and bottom panels correspond to  $\lambda = 1.55 \mu\text{m}$  and  $\lambda = 2.1 \mu\text{m}$ , respectively.

The temporal and spectral evolution of the pulse and FCs are presented in Figs. 3(a)–3(c). These plots show that after an initial stage in which the pulse broadens ( $z < 20 \text{ mm}$ ) a significant pulse compression is observed beyond  $z \simeq 20 \text{ mm}$ . It can be seen, however, that the pulse shape does not change periodically with  $z$ , which is due to the influence of effects other than the GVD and SPM. Specifically, TPA induces strong pulse decay whereas the TOD leads to pulse breakup. The effect of TPA on the pulse dynamics is particularly strong in the initial propagation stage during which, as Fig. 3(c) suggests, most of the pulse energy is absorbed by photogenerated FCs. Nevertheless, a maximum of more than fivefold pulse compression is achieved at  $z \simeq 60 \text{ mm}$ , which corresponds to a pulse duration of  $\sim 36 \text{ fs}$ . A common feature of pulses compressed via this method, which can also be seen in our simulations for  $z \gtrsim 60 \text{ mm}$ , is the generation of pedestals at the edges of the pulse.

In order to assess the degree to which the deleterious effects of TPA can be mitigated, we investigated the propagation of a secant-hyperbolic pulse in the mid-IR regime, namely at  $\lambda = 2.1 \mu\text{m}$ . The tapered wire considered in this case is defined by  $w_{\text{in}} = 850 \text{ nm}$ ,  $w_{\text{out}} = 750 \text{ nm}$ ,  $L = 3 \text{ cm}$ , and  $a = 80 \text{ m}^{-1}$ , the pulse parameters being  $\tau = 180 \text{ fs}$  and  $P_0 = 2.07 \text{ W}$  ( $N_s = 9$ ). Unlike the telecom case, the pulse decay is negligible at mid-IR wavelengths, its peak amplitude in fact increasing considerably. This substantial increase of the peak power, illustrated in Fig. 3(d), is explained by the fact that although part of the pulse energy is absorbed via TPA, the pulse undergoes significant compression as well, i.e., by more than  $10\times$  at  $z = 25 \text{ mm}$ , which should obviously result in increased peak power.

Unlike the case of optical fibers made of silica, photogenerated FCs can affect in a highly nontrivial way the dynamics of optical pulses that propagate in silicon wires. This idea is clearly illustrated by the plots in Figs. 3(c) and 3(f). Thus, whereas at  $\lambda = 1.55 \mu\text{m}$  the FC density decreases monotonously with  $z$ , at  $\lambda = 2.1 \mu\text{m}$  there is a certain propagation distance,  $z \simeq 20 \text{ mm}$ , at which a maximum amount of FCs is generated. This distance is roughly equal to the distance at which maximum pulse compression is observed. To understand this differ-

ence in pulse dynamics, note that at a given  $z$  the peak FC density can be estimated from Eq. (2) to be  $\Delta N(z) \simeq P^2(z)\Gamma''(z)\tau(z)/A^2(z)v_g^2(z)$ . Then, since the parameters  $\Gamma''$ ,  $A$ , and  $v_g$  vary only slightly with  $z$ , the main contribution to  $\Delta N(z)$  comes from the  $z$ -variation of the factor  $P^2(z)\tau(z) \sim P(z)E(z)$ . At mid-IR the pulse energy loss is rather small and therefore the maximum amount of FCs is generated when the peak power reaches its maximum, that is, when the pulse compression is maximum as well.

More insights into the pulse dynamics are provided by the semi-analytical model described by the system (5). By integrating numerically this system of equations we determined the dependence of the pulse parameters on the propagation distance, under the assumption that the pulse propagates in a particle-like manner. In an alternative approach, we computed the pulse parameters by fitting with a sech-function given by Eq. (4a) the pulse obtained by direct integration of the rigorous model (1)-(2). The results obtained by these two methods are represented in Fig. 4 by the black and blue lines, respectively. For comparison, the pulse parameters were also calculated by inserting in the definitions in Eq. (3) the solution obtained by numerical integration of the rigorous theoretical model (see the red curves in Fig. 4).

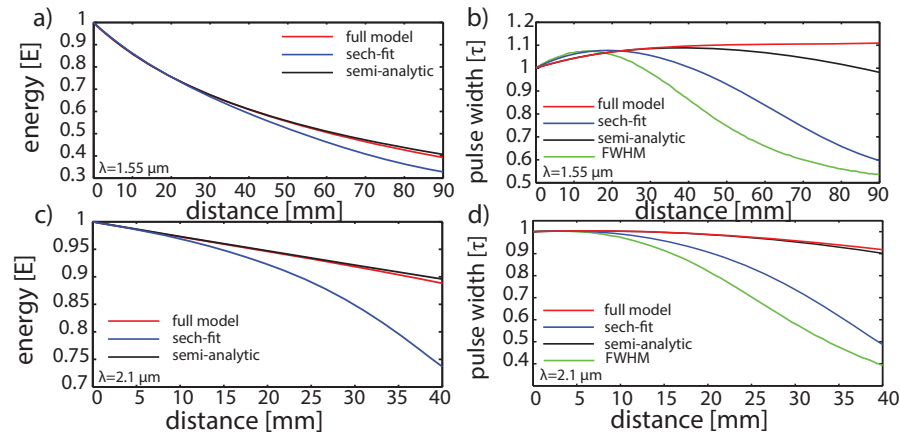


Fig. 4. Evolution of pulse energy  $E$  and width  $\tau$  vs. the propagation distance. Top panels correspond to  $\lambda = 1.55 \mu\text{m}$ ,  $\tau = 180 \text{ fs}$ , and  $P_0 = 0.2 \text{ W}$ , whereas the pulse parameters in the bottom panels are  $\lambda = 2.1 \mu\text{m}$ ,  $\tau = 180 \text{ fs}$ , and  $P_0 = 0.5 \text{ W}$ .

The results of this analysis, which are summarized in Fig. 4, show that, generally, there is a good agreement between the predictions of the full theoretical model and the semi-analytical model but only over a certain propagation distance. This proves that indeed in the initial stage of the propagation, the optical pulse can be viewed as a secant-hyperbolic pulse undergoing a particle-like dynamics. This approximation breaks down after a certain propagation distance ( $z \simeq 30 \text{ mm}$  at  $\lambda = 1.55 \mu\text{m}$  and  $z \simeq 10 \text{ mm}$  at  $\lambda = 2.1 \mu\text{m}$ ) as beyond this distance the optical pulse begins to split up. Our simulations (not shown here) suggest that, as expected, the distance over which the predictions of the full and semi-analytical models agree decreases with increasing  $P_0$ , since by increasing the nonlinearity one induces stronger pulse distortion. At both wavelengths, the pulse profile follows a similar evolution: initially the pulse broadens and then its width gradually decreases. To quantify the pulse compression after it breaks up, we determined its width by calculating the FWHM of the main pulse, as per the green curves in Fig. 4. It can be seen that, contrary to the predictions of the semi-analytical model, the main pulse is compressed significantly, which proves the effectiveness of tapered Si-PhWWGs in optical pulse reshaping applications.

To achieve a more complete understanding of the pulse compression mechanism, we also de-

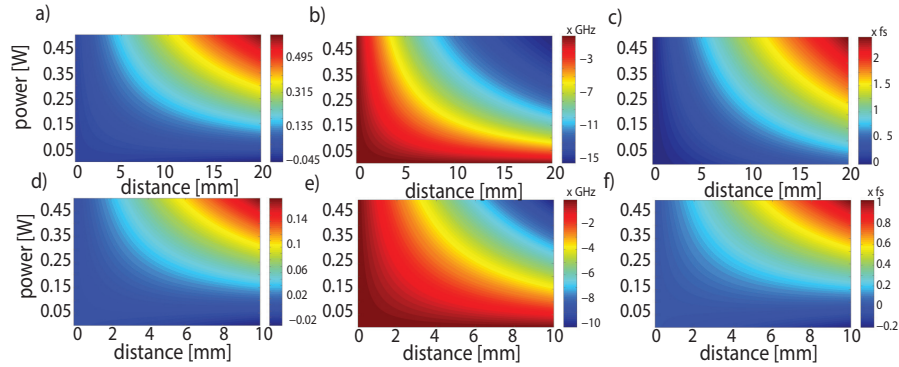


Fig. 5. Evolution of the pulse chirp  $C$  (left panels), frequency shift  $\Omega$  (middle panels), and temporal shift  $T$  (right panels), determined for different peak power. Top and bottom panels correspond to  $\lambda = 1.55 \mu\text{m}$  and  $\lambda = 2.1 \mu\text{m}$ , respectively, and throughout  $\tau = 180 \text{ fs}$ .

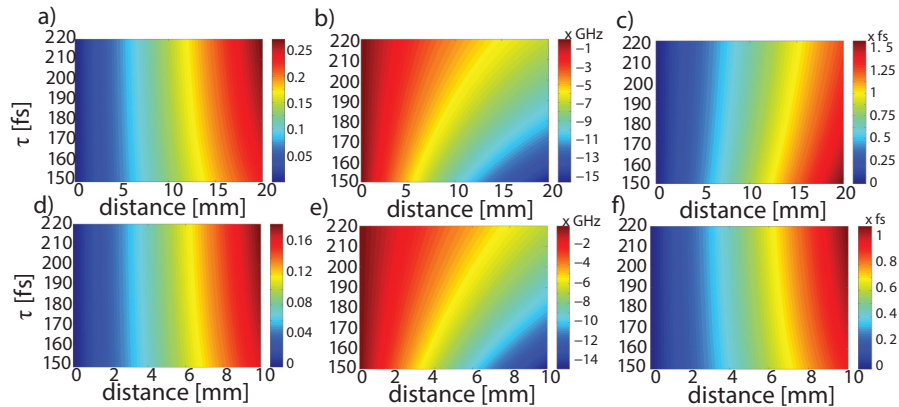


Fig. 6. The same as in Fig. 5, the pulse parameters being determined as function of  $\tau$ . The pulse power in the top and bottom panels is  $P_0 = 1.4 \text{ W}$  and  $P_0 = 2.07 \text{ W}$ , respectively.

terminated the  $z$ -dependence of the chirp,  $C(z)$ , center frequency shift,  $\Omega(z)$ , and temporal shift,  $T(z)$ , calculated as function of the input pulse peak power  $P_0$  and width  $\tau$ . The corresponding results are presented in Figs. 5 and 6, respectively. Note that these numerical simulations were performed for a range of pulse parameters and propagation distance where the semi-analytical model agrees well with the rigorous one, so that these parameters have a meaningful physical interpretation. Figures 5 and 6 show that, except for relatively small peak power, the chirp is positive and increases monotonously with  $z$ , that is the positive chirp generated by SPM is larger than the negative one generated by the anomalous GVD. As a result, the initial propagation stage in which the pulse broadens is followed by a monotonous pulse compression. This is the expected behavior of a pulse that propagates in the anomalous GVD regime, the  $z$ -dependence of the pulse chirp explaining why the pulse compression is preceded by an initial pulse broadening. Thus, initially the pulse broadens under the influence of the GVD, but as the positive chirp induced by the SPM increases, the GVD begins to have an opposite effect, namely it compresses the pulse. As the pulse is compressed, the GVD and the peak power increase. Therefore, the SPM and, consequently, the rate at which the chirp increases become larger, too, which further increases the efficiency of the pulse compression process. A similar

monotonous increase with the propagation distance, albeit extremely small ( $T \simeq 1$  fs), is shown by the pulse temporal shift. This effect, whose magnitude is comparable to  $\tau_s$ , is due to the frequency dispersion of the nonlinearity and the TOD. Finally, the center frequency of the pulse is redshifted, the magnitude of this redshift increasing with  $z$ . As expected, the magnitude of the frequency shift increases with the peak power,  $P_0$  (the strength of the nonlinearity dispersion increases with  $P_0$ ) and decreases with the pulse width,  $\tau$  (TOD increases as  $\tau$  decreases).

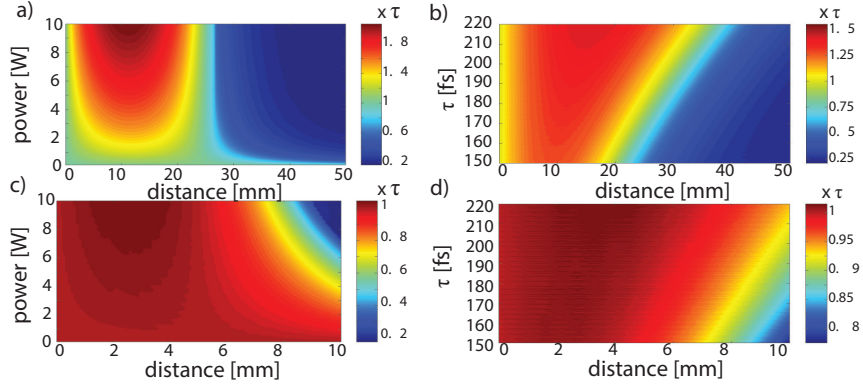


Fig. 7. a) Dependence of the pulse width on  $P_0$ , determined for  $\tau = 180$  fs and b) on  $\tau$ , determined for  $P_0 = 1.4$  W. c) Dependence of the pulse width on  $P_0$ , determined for  $\tau = 180$  fs and d) on  $\tau$ , determined for  $P_0 = 2.07$  W. The top and bottom plots correspond to  $\lambda = 1.55 \mu\text{m}$  and  $\lambda = 2.1 \mu\text{m}$ , respectively. The color bar indicates the pulse width, normalized to its initial value.

Since this study is concerned primarily with the investigation of pulse compression mechanisms in tapered Si-PhWWGs and the physical effects that determine their efficiency, we provide now a more detailed description of the dependence of the pulse compression factor on the pulse power and width. This is a natural choice of pulse parameters as the main characteristic lengths that govern the pulse propagation, the linear and nonlinear lengths, depend solely on  $\tau$  and  $P_0$ . The results of this investigation are summarized in Fig. 7. Thus, comparing the results presented in the top and bottom panels in Fig. 7, one can see that the pulse compression is much more efficient at mid-IR, namely a shorter propagation distance is needed to achieve a certain compression factor. This can be easily explained using the characteristics of the pulse evolution we just discussed: the TPA is much weaker at mid-IR, which means that the positive SPM-induced chirp and hence the pulse compression is much larger in this frequency domain. Moreover, the maps plotted in Fig. 7 show that the compression factor increases with  $P_0$  but decreases with  $\tau$ . This finding has a simple explanation, namely whereas the SPM is proportional to  $P_0$ , the strength of GVD effects is inverse proportional to  $\tau^2$ . Note, however, that if only waveguide tapering effects are considered then both SPM and GVD increase with the propagation distance, as for the two tapers considered in this section  $\gamma$  and  $|\beta_2|$  increase with  $z$ .

This analysis suggests that, surprisingly, pulse compression can be achieved even when the dispersion increases. To be more specific, previous studies of adiabatic soliton compression in dispersion-managed optical fibers have demonstrated that pulse compression in lossless fibers with constant nonlinearity can be achieved only if  $|\beta_2|$  decreases. Indeed, under these circumstances, for the soliton number  $N_s^2 = \gamma P_0 \tau^2 / |\beta_2|$  to remain constant while the pulse duration,  $\tau$ , decreases, the GVD coefficient  $|\beta_2|$  must decrease as well. In tapered Si-PhWWGs, however, the increase of the GVD coefficient can be offset by the increase of  $\gamma$  ( $\gamma$  increases as the waveguide width decreases, as per Fig. 2), so that soliton pulse compression can be achieved even in

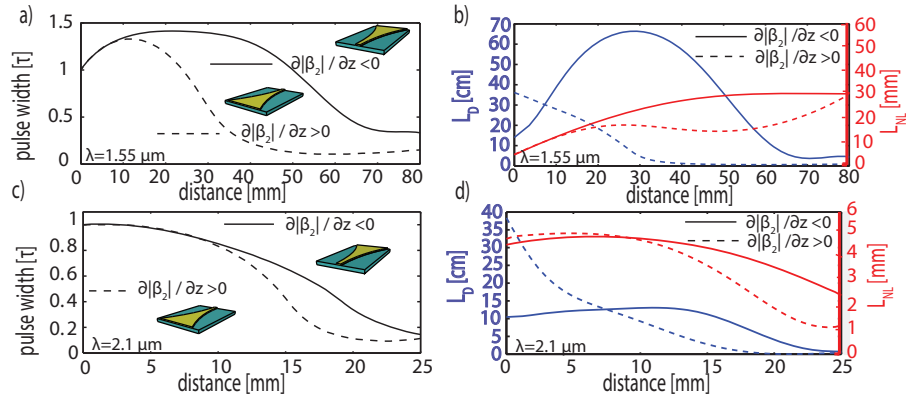


Fig. 8. Evolution of pulse width (left panels) and  $L_D$  and  $L_{nl}$  (right panels) determined for tapered Si-PhWWGs with increasing (dotted line) and decreasing (solid line) dispersion.

dispersion-increasing tapered waveguides.

These ideas are illustrated in Fig. 8, where we show the dependence of the pulse width on the propagation distance in tapers with increasing as well as decreasing dispersion. Note that the pulse width presented in this figure is calculated by evaluating the FWHM of the main part of the pulse. Thus, we launch a pulse with  $P_0 = 1.4$  W ( $P_0 = 2.07$  W) in a tapered Si-PhWWGs with  $w_{in} = 700$  nm ( $w_{in} = 850$  nm),  $w_{out} = 660$  nm ( $w_{out} = 750$  nm), and  $L = 90$  mm ( $L = 30$  mm), the wavelength being  $\lambda = 1.55$   $\mu\text{m}$  ( $\lambda = 2.1$   $\mu\text{m}$ ). In both cases  $\tau = 180$  fs and  $a = 80$  m $^{-1}$ . The  $z$ -dependence of the pulse width, as well as that of  $L_D$  and  $L_{nl}$ , are depicted in Fig. 8 with dotted lines. The solid lines in this figure correspond to the pulse propagation in the inverted taper, namely to the case in which the roles of  $w_{in}$  and  $w_{out}$  are interchanged while the pulse parameters are kept unchanged. As a result, in the first case the GVD dispersion increases (in absolute value), whereas the latter one corresponds to decreasing dispersion. Nevertheless, in both cases, the soliton is significantly compressed, as per Figs. 8(a) and 8(c). A closer look at the interplay between the two main characteristic lengths defining the soliton dynamics leads us to the same conclusion. More specifically, Figs. 8(b) and 8(d) show that for both tapers  $L_D > L_{nl}$ , which means that the nonlinear effects are stronger. A consequence of this fact is that, as discussed above, the total chirp is positive. As the pulse propagates in the anomalous GVD regime, this results in pulse compression.

From a more practical point of view, it is important to understand to what degree the taper profile affects the efficiency of the pulse compression. While we did not try to find the optimum taper profile that leads to maximum compression, we have considered the pulse propagation in hyperbolically and linearly tapered Si-PhWWGs, that is, two of the commonly used taper profiles. The  $z$ -profile of the linear taper is defined by  $w(z) = w_{in} - (w_{in} - w_{out})z/L$ . The input and output widths as well as the waveguide length were the same for both types of tapers: at  $\lambda = 1.55$   $\mu\text{m}$ ,  $w_{in} = 700$  nm,  $w_{out} = 660$  nm, and  $L = 90$  mm, whereas at  $\lambda = 2.1$   $\mu\text{m}$ ,  $w_{in} = 850$  nm,  $w_{out} = 750$  nm, and  $L = 30$  mm. The pulse peak power was  $P_0 = 1.4$  W ( $P_0 = 2.07$  W) at  $\lambda = 1.55$   $\mu\text{m}$  ( $\lambda = 2.1$   $\mu\text{m}$ ), whereas in both cases  $\tau = 180$  fs and  $a = 80$  m $^{-1}$ . The results of our analysis, summarized in Fig. 9, suggest that whereas the pulse width follows a similar evolution as it propagates in the two tapers, specific differences lead us to conclude that the hyperbolic taper is more efficient for pulse compression. Interestingly enough, similar conclusions were reached when Gaussian pulses with the same power and width were used. This finding can be explained by the fact that in the case of the hyperbolic taper there is a more rapid transition to the waveguide region with large nonlinearity, as compared to the case of the

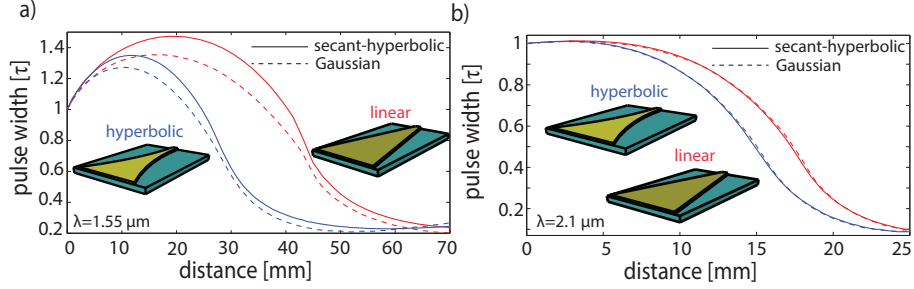


Fig. 9. a) Evolution of the pulse width for two taper profiles, calculated for  $P_0 = 1.4 \text{ W}$  and  $\lambda = 1.55 \mu\text{m}$  and b) for  $P_0 = 2.07 \text{ W}$  and  $\lambda = 2.1 \mu\text{m}$ . In both cases the initial pulse width is  $\tau = 180 \text{ fs}$ .

linear taper, which means that the generated positive chirp that induces pulse compression is larger in the former case.

## 5. Pulse compression below the soliton power threshold

One of the conclusions of the preceding section is that large pulse compression factor can be achieved when an optical pulse with positive chirp propagates in the anomalous GVD regime. One drawback of this approach is that if  $\beta_2 < 0$  the chirp induced by the GVD is negative and hence reduces the positive chirp generated by the SPM. One possible solution to this problem, which can be easily implemented by using adiabatically tapered Si-PhWWGs, is to first propagate the pulse in a section of the waveguide with large normal GVD until the pulse accumulates a large positive chirp and then propagate this chirped pulse in a waveguide section with large anomalous GVD, where the pulse is compressed. In a practical setting, this scheme can be implemented by simply using a tapered Si-PhWWG whose width is varied in such a way that the waveguide has normal and anomalous GVD within its input and output sections, respectively [see also Fig. 1(b)]. It should be mentioned that this pulse compression method can be applied to pulses with low peak power as well, as it does not require that the pulse propagates in the soliton regime. The larger the power, however, the larger the compression factor will be because a larger positive chirp would be generated within the waveguide section with normal GVD.

The semi-analytical model described by Eq. (5) provides an intuitive picture of this pulse compression mechanism. Thus, if one considers a secant-hyperbolic pulse given by Eq. (4a) and neglects TPA effects and the higher-order terms in Eq. (1), that is,  $\gamma'' = 0$ ,  $\beta_3 = 0$ , and  $\tau_s = 0$ , Eqs. (8b) and (8c) become (see also [49]):

$$\frac{d\tau}{dz} = \frac{\beta_2 C}{\tau}, \quad (6a)$$

$$\frac{dC}{dz} = \left( \frac{4}{\pi^2} + C^2 \right) \frac{\beta_2}{\tau^2} + \frac{2\gamma' E}{\pi^2 \tau}, \quad (6b)$$

where the pulse energy,  $E$ , is conserved upon propagation. This system of equations shows that when the pulse propagates in the waveguide section with normal GVD,  $\beta_2 > 0$ , both terms in the rhs of Eq. (6b) contribute to the increase of the chirp. When subsequently the pulse propagates in the waveguide section with anomalous GVD,  $\beta_2 < 0$ , the rhs of Eq. (6a) is negative, and therefore the optical pulse is compressed. This system of equations also suggests that the larger is the chirp generated in the first section of the waveguide the larger will be the overall pulse compression factor.

To illustrate these ideas, we considered the propagation of optical pulses in tapered Si-PhWWGs whose dispersion changes from normal to anomalous. For this, we considered two tapered Si-PhWWGs defined by the following parameters:  $w_{\text{in}} = 850$  nm and  $w_{\text{out}} = 610$  nm, at  $\lambda = 1.55$   $\mu\text{m}$ , and  $w_{\text{in}} = 980$  nm and  $w_{\text{out}} = 735$  nm, at  $\lambda = 2.1$   $\mu\text{m}$ . In both cases  $a = 80$   $\text{m}^{-1}$ ,  $L = 90$  mm, and  $\tau = 180$  fs, whereas the pulse power was  $P_0 = 90$  mW at  $\lambda = 1.55$   $\mu\text{m}$  and  $P_0 = 100$  mW at  $\lambda = 2.1$   $\mu\text{m}$ . This choice of waveguide and pulse parameters means that  $N_s(z = 0) = 0.895 < 1$  at  $\lambda = 1.55$   $\mu\text{m}$  and  $N_s(z = 0) = 0.908 < 1$  at  $\lambda = 2.1$   $\mu\text{m}$ . While solitons do not exist in the normal GVD regime, the soliton number allows us to compare the compression factor that can be achieved by the two methods, at specific peak powers.

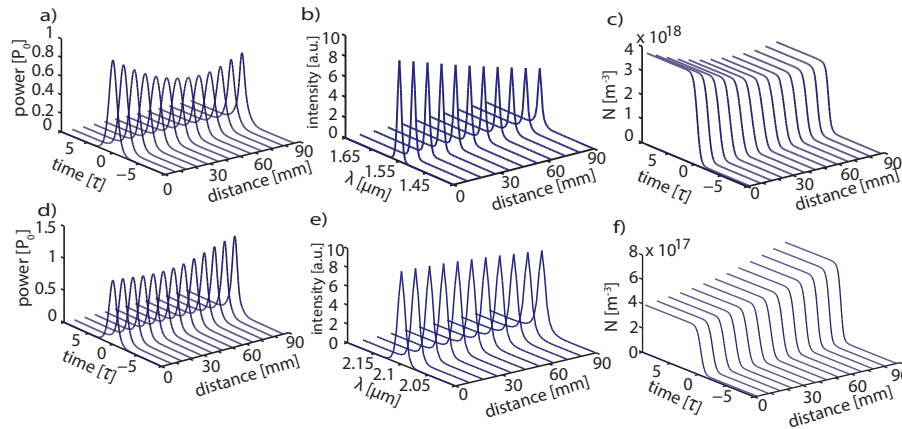


Fig. 10. Temporal [a) and d)] and spectral [b) and e)] pulse evolution in a tapered Si-PhWWGs whose dispersion changes from normal to anomalous (see text for taper and pulse parameters) and the corresponding free-carriers dynamics [c) and f)]. Top and bottom panels correspond to  $\lambda = 1.55$   $\mu\text{m}$  and  $\lambda = 2.1$   $\mu\text{m}$ , respectively.

The evolution of the temporal and spectral profile of the pulse, as well as that of FC-density, at both wavelengths, are presented in Fig. 10. This figure shows that the pulse is compressed at both wavelengths; however, the compression factor is smaller than in the case of soliton compression, chiefly because the peak power is significantly smaller in this case. In addition, as expected, TPA has different impact on the pulse compression at the two wavelengths. At  $\lambda = 1.55$   $\mu\text{m}$ , where the TPA is large, the pulse propagates in a lossy medium and therefore its width initially increases, before undergoing compression in the waveguide section with  $\beta_2 < 0$ , namely beyond  $z \simeq 40$  mm. By contrast, at  $\lambda = 2.1$   $\mu\text{m}$  the TPA is weak, so that the width of the pulse remains approximately constant for  $z \lesssim 30$  mm and then begins to decrease. Since the peak power is relatively small in this case, the amount of generated FCs is small as well (compare the FC-densities in Figs. 3 and 10) and consequently the  $z$ -dependence of FCs is similar to that of the pulse power.

A more quantitative characterization of the pulse compression is presented in Fig. 11, where we show the evolution of the pulse width vs. the propagation distance. Thus, it can be seen that the pulse broadens while it propagates in the section of the waveguide with normal GVD (the zero-GVD point is located at  $z = 30$  mm) and subsequently undergoes significant compression. In particular, the pulse width decreases by 29% at  $\lambda = 1.55$   $\mu\text{m}$  and by 27% at  $\lambda = 2.1$   $\mu\text{m}$ , after a total propagation distance of 90 mm. The input pulse width is  $\tau = 180$  fs and the input power is  $P_0 = 90$  mW at  $\lambda = 1.55$   $\mu\text{m}$  and  $P_0 = 100$  mW at  $\lambda = 2.1$   $\mu\text{m}$ , which ensures that  $N_s(z = 0) < 1$ , namely the peak power of the input pulse is smaller than the soliton formation threshold. However, as the pulse approaches the zero-GVD point,  $N_s$  increases considerably

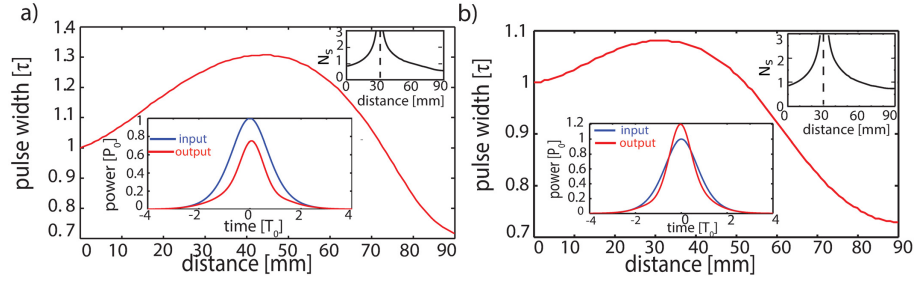


Fig. 11. Evolution of the pulse width upon propagation in a tapered Si-PhWWGs whose dispersion changes from normal to anomalous, determined for a)  $\lambda = 1.55 \mu\text{m}$  and b)  $\lambda = 2.1 \mu\text{m}$ . Insets depict the evolution of the soliton number  $N_s$  as well as the input and output pulse profiles.

since  $\beta_2$  becomes very small ( $N_s \rightarrow \infty$  as  $|\beta_2| \rightarrow 0$ ). After the pulse passes through the zero-GVD point  $N_s$  begins to decrease and becomes again less than 1 in the final propagation stage.

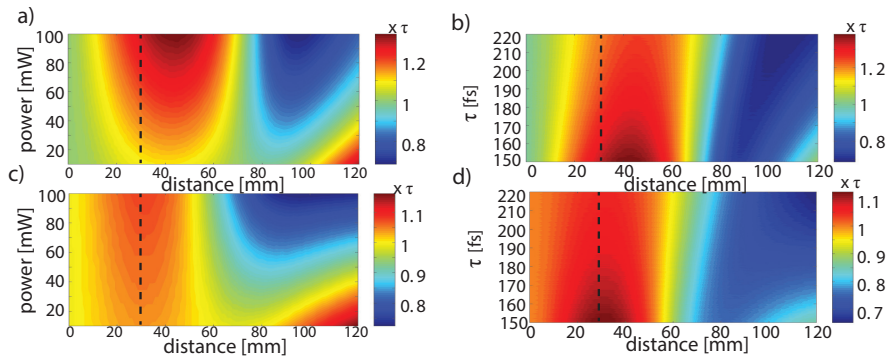


Fig. 12. a) Dependence of the pulse width vs. peak power  $P_0$ , determined for  $\tau = 180$  fs, and b) vs.  $\tau$ , determined for  $P_0 = 90$  mW. c) Dependence of the pulse width vs. peak power  $P_0$ , determined for  $\tau = 180$  fs and d) vs.  $\tau$ , determined for  $P_0 = 100$  mW. Top and bottom panels correspond to  $\lambda = 1.55 \mu\text{m}$  and  $\lambda = 2.1 \mu\text{m}$ , respectively. The color bar indicates the pulse width, normalized to its initial value, whereas the vertical dashed lines indicate the distance at which  $\beta_2 = 0$ .

The dependence of the compression factor on the pulse parameters, determined for the same pair of tapers as that corresponding to Fig. 10 but with  $L = 120$  mm, is summarized in Fig. 12. Note that we chose the input power in these simulations such that the soliton number remains smaller than 1 for the most part of the propagation. The main conclusion illustrated by these plots is that pulse compression can be achieved for a broad spectrum of pulse widths and powers. For all values of the pulse parameters one requires a certain propagation distance (waveguide length) in order to achieve pulse compression, as initially the pulse broadens. It can also be seen that the compression factor depends rather weakly on the pulse parameters and the operation wavelength. In particular, for a given propagation distance, the compression factor increases with the pulse power and decreases with the pulse width. This conclusion can be derived from the dependence on the pulse parameters of the SPM and GVD chirps, namely, as suggested by Eq. (6b), the SPM chirp increases with the pulse power whereas the GVD chirp increases when the pulse width decreases.

## 6. Conclusion

In conclusion, we have demonstrated that tapered silicon photonic wire waveguides provide convenient, easy to implement solutions for optical pulse compression at optical-chip scale. By taking advantage of the strong dependence of the linear and nonlinear optical coefficients of a silicon waveguide on its transverse cross-section one can easily tailor the variation along the waveguide of the frequency dispersion and waveguide nonlinearity, so that the temporal and spectral properties of optical pulses can be reshaped in a pre-designed, controlled way. We considered two pulse compression mechanisms, one that applies to optical pulses that propagate in the soliton regime, and a more general one employing waveguides with sign-changing dispersion, which can be used to compress low-power pulses as well. We demonstrated that while the former method can be used only for pulses that propagate in the anomalous GVD regime, it is significantly more efficient than the latter one, compression factors as large as 10 being readily achievable. A detailed analysis and discussion of the relationship between the compression factors that can be achieved by using either one of the two methods and the pulse width and power as well as the profile of the taper have also been presented.

### Appendix: Mathematical formulation of the semi-analytical model

By taking the  $z$ -derivatives of the pulse parameters defined in Eqs. (3a)–(3e) and inserting Eq. (1), in which the first two terms in the rhs are neglected, into the resulting integrals, simple but lengthy mathematical manipulations lead to the following system of nonlinear ordinary differential equations that describes the evolution of the pulse parameters:

$$\frac{dE}{dz} = -2(\gamma)'' \int_{-\infty}^{\infty} |u|^4 dt - 4 \int_{-\infty}^{\infty} |u|^2 (\gamma\tau_s u^* u_t)' dt - 2 \int_{-\infty}^{\infty} |u|^2 (\gamma\tau_s u u_t^*)' dt, \quad (7a)$$

$$\begin{aligned} \frac{d\tau}{dz} = & -\frac{\delta}{2\tau E^2} \frac{dE}{dz} \int_{-\infty}^{\infty} (t-T)^2 |u|^2 dt - \frac{\delta}{2\tau E} \frac{dT}{dz} \int_{-\infty}^{\infty} (t-T) |u|^2 dt + \frac{\pi^2 \delta}{12} \beta_2 \frac{C}{\tau} \\ & + \frac{\delta \beta_3}{2\tau E} \int_{-\infty}^{\infty} (t-T) |u_t|^2 dt - \frac{2\delta}{E\tau} \int_{-\infty}^{\infty} (t-T)^2 |u|^2 (\gamma\tau_s u^* u_t)' dt \\ & - \frac{\delta \gamma''}{\tau E} \int_{-\infty}^{\infty} (t-T)^2 |u|^4 dt - \frac{\delta}{\tau E} \int_{-\infty}^{\infty} (t-T)^2 |u|^2 (\gamma\tau_s u u_t^*)' dt, \end{aligned} \quad (7b)$$

$$\begin{aligned} \frac{dC}{dz} = & \frac{\delta \beta_2}{E} \int_{-\infty}^{\infty} |u_t|^2 dt + \frac{i\delta \beta_3}{4E} \int_{-\infty}^{\infty} (u_{tt} u_t^* - u_{tt}^* u_t) dt \\ & - \frac{2\delta}{E} \int_{-\infty}^{\infty} (t-T) |u|^2 (\gamma u^* u_t)' dt - \frac{2\delta}{E} \int_{-\infty}^{\infty} (t-T) [\gamma\tau_s u_t^* (|u|^2 u_t)]'' dt \\ & - \frac{2\delta}{E} \int_{-\infty}^{\infty} |u|^2 (\gamma\tau_s u^* u_t)'' dt - \frac{\delta}{E} \int_{-\infty}^{\infty} |u|^2 (\gamma\tau_s u u_t^*)'' dt \\ & - \frac{i\delta}{2E^2} \frac{dE}{dz} \int_{-\infty}^{\infty} (t-T) (u^* u_t - u u_t^*) dt - \frac{i\delta}{2E} \frac{dT}{dz} \int_{-\infty}^{\infty} (u^* u_t - u u_t^*) dt, \end{aligned} \quad (7c)$$

$$\begin{aligned} \frac{d\Omega}{dz} = & -\frac{i}{2E^2} \frac{dE}{dz} \int_{-\infty}^{\infty} (u^* u_t - u u_t^*) dt - \frac{2}{E} \int_{-\infty}^{\infty} (\gamma u^* u_t)' |u|^2 dt \\ & - \frac{4(\gamma\tau_s)''}{E} \int_{-\infty}^{\infty} |u u_t|^2 dt - \frac{2}{E} \int_{-\infty}^{\infty} [\gamma\tau_s (u u_t^*)^2]'' dt, \end{aligned} \quad (7d)$$

$$\begin{aligned} \frac{dT}{dz} = & -\frac{1}{E^2} \frac{dE}{dz} \int_{-\infty}^{\infty} t |u|^2 dt + \beta_2 \Omega + \frac{\beta_3}{2E} \int_{-\infty}^{\infty} |u_t|^2 dt - \frac{2\gamma''}{E} \int_{-\infty}^{\infty} t |u|^4 dt \\ & - \frac{4}{E} \int_{-\infty}^{\infty} t |u|^2 (\gamma\tau_s u^* u_t)' dt - \frac{2}{E} \int_{-\infty}^{\infty} t |u|^2 (\gamma\tau_s u u_t^*)' dt. \end{aligned} \quad (7e)$$

This nonlinear system of equations depends on the specific pulse shape,  $u(z, t)$ . For secant-hyperbolic pulses given by Eq. (4a)  $\delta = 12/\pi^2$ , so that this system reads,

$$\frac{dE}{dz} = -\frac{2\gamma''E^2}{3\tau} - \frac{2(\gamma\tau_s)''E^2\Omega}{3\tau}, \quad (8a)$$

$$\frac{d\tau}{dz} = (\beta_2 + \beta_3\Omega)\frac{C}{\tau} + \frac{\pi^2 - 6}{3\pi^2} [-\gamma'' - (\gamma\tau_s)''\Omega]E - \frac{\tau}{2E}\frac{dE}{dz}, \quad (8b)$$

$$\begin{aligned} \frac{dC}{dz} = & \beta_2 \left[ \left( \frac{4}{\pi^2} + C^2 \right) \frac{1}{\tau^2} + \frac{12\Omega^2}{\pi^2} \right] + \beta_3 \left[ \left( \frac{2}{\pi^2} + \frac{3C^2}{2} \right) \frac{\Omega}{\tau^2} + \frac{6\Omega^3}{\pi^2} \right] - \frac{C}{E}\frac{dE}{dz} - \Omega\frac{dT}{dz} \\ & - \frac{2(\pi^2 - 6)}{3\pi^2} \left[ \gamma'' + \frac{\pi^2}{6}(\gamma\tau_s)''\Omega \right] \frac{EC}{\tau} + \frac{2}{\pi^2} \left[ \gamma' + \frac{\pi^2 + 12}{6}(\gamma\tau_s)'\Omega \right] \frac{E}{\tau}, \end{aligned} \quad (8c)$$

$$\frac{d\Omega}{dz} = \frac{1}{3} \left[ -2\gamma''\Omega + (\gamma\tau_s)'\frac{C}{\tau^2} - (\gamma\tau_s)'' \left( \frac{6}{5\tau^2} + 2\Omega^2 + \frac{\pi^2 - 6}{6}\frac{C^2}{\tau^2} \right) \right] \frac{E}{\tau} - \frac{\Omega}{E}\frac{dE}{dz}, \quad (8d)$$

$$\begin{aligned} \frac{dT}{dz} = & \beta_2\Omega + \frac{\beta_3}{2} \left[ \frac{1}{3\tau^2} + \Omega^2 + \frac{\pi^2 C^2}{12\tau^2} \right] - \left[ \frac{2}{3}\gamma''T - \frac{(\gamma\tau_s)'}{2} \right] \frac{E}{\tau} \\ & - \frac{(\gamma\tau_s)''}{3} \left( 2T\Omega + \frac{\pi^2 - 6}{6}C \right) \frac{E}{\tau} - \frac{T}{E}\frac{dE}{dz}, \end{aligned} \quad (8e)$$

whereas  $\delta = 2$  in the case of Gaussian pulses given by Eq. (4b), so that (7) becomes,

$$\frac{dE}{dz} = -\sqrt{\frac{2}{\pi}}\frac{\gamma''E^2}{\tau} - \sqrt{\frac{2}{\pi}}\frac{(\gamma\tau_s)''E^2\Omega}{\tau}, \quad (9a)$$

$$\frac{d\tau}{dz} = (\beta_2 + \beta_3\Omega)\frac{C}{\tau} - \frac{1}{\sqrt{8\pi}} [\gamma'' + (\gamma\tau_s)''\Omega]E - \frac{1}{2}\frac{\tau}{E}\frac{dE}{dz}, \quad (9b)$$

$$\begin{aligned} \frac{dC}{dz} = & \beta_2 \left[ (1 + C^2) \frac{1}{\tau^2} + 2\Omega^2 \right] + \beta_3 \left[ (1 + 3C^2) \frac{\Omega}{2\tau^2} + \Omega^3 \right] - \frac{C}{E}\frac{dE}{dz} - \Omega\frac{dT}{dz} \\ & - \frac{1}{\sqrt{2\pi}} [\gamma'' + 2(\gamma\tau_s)''\Omega] \frac{EC}{\tau} + \frac{1}{\sqrt{2\pi}} [\gamma' + 2(\gamma\tau_s)'\Omega] \frac{E}{\tau}, \end{aligned} \quad (9c)$$

$$\frac{d\Omega}{dz} = \frac{1}{\sqrt{2\pi}} \left[ -2\gamma''\Omega + (\gamma\tau_s)'\frac{C}{\tau^2} - (\gamma\tau_s)'' \left( \frac{3}{2\tau^2} + 2\Omega^2 + \frac{1}{2}\frac{C^2}{\tau^2} \right) \right] \frac{E}{\tau} - \frac{\Omega}{E}\frac{dE}{dz}, \quad (9d)$$

$$\begin{aligned} \frac{dT}{dz} = & \beta_2\Omega + \frac{\beta_3}{2} \left[ \frac{1}{2\tau^2} + \Omega^2 + \frac{1}{2}\frac{C^2}{\tau^2} \right] - \frac{1}{\sqrt{2\pi}} \left[ 2\gamma''T - \frac{3(\gamma\tau_s)'}{2} \right] \frac{E}{\tau} \\ & - \sqrt{\frac{2}{\pi}}(\gamma\tau_s)'' \left( T\Omega + \frac{C}{4} \right) \frac{E}{\tau} - \frac{T}{E}\frac{dE}{dz}. \end{aligned} \quad (9e)$$

By eliminating the derivatives  $\frac{dE}{dz}$  and  $\frac{dT}{dz}$  from the rhs of Eqs. (8) and (9), these systems of equations become equivalent to Eq. (5).

### Acknowledgments

The work of S. L. was supported through a UCL Impact Award graduate studentship. R. R. G. acknowledges support from the Columbia Optics and Quantum Electronics IGERT under NSF Grant DGE-1069420.